Journal of Energy Chemistry 115 (2026) 65–75

Contents lists available at ScienceDirect

Journal of Energy Chemistry

journal homepage: www.elsevier.com/locate/jechem

http://www.journals.elsevier.com/journal-of-energy-chemistry/

Delocalizing excited states of entangled dual-acceptor phases consolidates donor-dilute semitransparent organic solar cells

Xiaoxiao Zhang [a], Zhiyuan Wu [a], Jiaqi Xie [a], Weihua Lin [b], Kaibo Zheng [c,*], Ziqi Liang [a,d,*]

[a] College of Smart Materials and Future Energy, Fudan University, Shanghai 200438, China
[b] MAX IV Laboratory, Lund University, P.O. Box 118, 22100 Lund, Sweden
[c] Department of Chemical Physics and NanoLund, Lund University, Box 124, 22100 Lund, Sweden
[d] State Key Laboratory of Photovoltaic Science and Technology, Fudan University, Shanghai 200438, China

ARTICLE INFO

Article history:
Received 10 November 2025
Accepted 14 November 2025
Available online 19 November 2025

Keywords:
Donor dilute
Excited states
Entangled dual-acceptor phases
Exciton dissociation
Semitransparent organic solar cells

ABSTRACT

Organic semiconductors are uniquely featured with narrow optical bands that allow them to exhibit selective near-infrared absorption compared to silicon and halide perovskite analogues, making them a favorite for constructing semitransparent photovoltaics. Often, achieving a high power conversion efficiency while maintaining an excellent visible light transmittance remains a grand challenge. In semitransparent organic solar cells (ST-OSCs), the donor-dilute strategy offers a simpler means than incorporating optical coupling layers to strike a delicate balance between transparency and efficiency, yet facing the issues of exciton splitting and hole transfer. This study newly incorporates a polymer acceptor PYIT into an optimal PM6(30 wt%):L8-BO blend to form entangled dual-acceptor phases and delocalize excited states, which promote exciton dissociation and elongate exciton lifetime within the acceptor phases, thus reducing the dependence on donor/acceptor interfaces for charge separation. By further substitution with a lower-bandgap PTB7-Th donor layer and a better hole-selective layer of [2-(9H-carbazol-9-yl)ethyl]phosphonic acid (2PACz) while introducing an antireflective layer of TeO_2 to enhance device transparency, the overall light utilization efficiency reached a champion 5.63%. This contribution represents an environmentally benign, operationally scalable, and universally applicable strategy, offering practical prospects for future sustainable building-integrated photovoltaic systems.

1. Introduction

Organic solar cells are conceived as one of the most popular clean energy technologies thanks to their unique merits such as the green and modifiable molecular structures, solution processing, and large-area roll-to-roll manufacturing [1–5]. Remarkably, nonfullerene-acceptor organic solar cells (NF-OSCs) have now witnessed a great breakthrough with power conversion efficiencies (PCEs) beyond 20% [6], affording high competitiveness with silicon and halide perovskite-based solar cells [7,8]. Unlike the characteristics of their counterparts of full-spectrum light absorbance [9–11], organic photoactive semiconductors are featured with narrow optical absorption and photoluminescence bands, which can readily red-shift beyond the visible range into the near-infrared (NIR) region via molecular tailoring [12,13]. The exquisitely tunable absorption characteristics of organic semiconductors endow semi-transparent organic solar cells (ST-OSCs) with the capability of functioning as power-generating windows featuring an extraordinarily high level of visible transmittance. This unique property allows ST-OSCs to enhance average visible transmittance (AVT) while maintaining high PCEs of the devices, thus combining energy generation with visible-light transmission for applications in building-integrated photovoltaics, vehicular glazing, and agrivoltaics [14–18].

Typically, the PCE of ST-OSCs increases with the decrease of AVT, for which the light utilization efficiency (that is, LUE = PCE × AVT) is coined to assess a balance between those two terms [19,20]. To date, the best-performing ST-OSCs have reached LUEs of over 6% [21–23]. Besides, the color rendering index (CRI) is utilized to assess the color rendering capabilities of ST-OSCs; that is, a high CRI value indicates a superior ability to portray the real color of an object, which reflects the shape of the visible spectrum

* Corresponding authors.
E-mail addresses: kaibo.zheng@chemphys.lu.se (K. Zheng), zqliang@fudan.edu.cn (Z. Liang).

https://doi.org/10.1016/j.jechem.2025.11.015

instead of the function of AVT [24]. As a result, the ST-OSCs with both high LUE and CRI values are worthy to be investigated in detail.

To fabricate ST-OSCs, transparent electrodes are not only a necessity but also a key component in the overall device design [7,25–27]. They must be integrated into a carefully engineered system that balances light absorption, electrical conductivity, and optical transparency to achieve the best performance for the ST-OSCs. As one example, Li et al. designed a thin, semitransparent, and high-conductivity 2% Cu/Ag alloy electrode, which was combined with optical outcoupling (OOC) and antireflection coatings (ARC), resulting in a significant increase in LUE [28]. Taken another, Deng et al. developed an optimized ARC, consisting of a Na_3AlF_6 (160 nm)/ZnSe (190 nm) bilayer, to enhance transmission in the visible wavelength range (400–600 nm) and strengthen reflection intensity in the NIR wavelength (780–2500 nm) [29]. However, constructing OOC and ARC is an intimidating task, which will pose a series of complex processing challenges.

A complementary and more crucial avenue to ST-OSCs is to regulate light absorption of the active layer in the visible spectrum. In benchmark NF-OSCs, the absorption bands of donors and acceptors are concentrated in the visible (300–700 nm) and NIR (600–1000 nm) regions, respectively. Therefore, donor dilution has become a straightforward and effective strategy for fabricating high-performance ST-OSCs [7,30–32]. Declining the content of donors in the active layer elevates AVT, however, resulting in a sequence of challenges: (1) the reduction in photon utilization in the visible spectrum leads to a loss of short-circuit current density (J_{SC}); (2) the reduced continuity of the donor phases will impede hole transport; (3) the decrease in donor/acceptor (D/A) interfaces could hinder exciton dissociation.

To address the first issue, current research favored the incorporation of a third component to enhance J_{SC} [22,30,33–35]. For instance, Chen and coworkers introduced a small-molecule acceptor BTP-eC9 into PBDB-TF:L8-BO host blend films, which extended the absorption spectra of active layers towards the NIR region, resulting in a 5% increase in J_{SC} [36]. Second, the discontinued donor phase hindered hole transfer, thus interfering with the balance of electron and hole transport and inducing space-charge effects. This can ultimately culminate in a substantial increase in bimolecular recombination. Our previous work incorporated a tiny amount (0.005 wt%) of n-type dopant 4-(1,3-dimethyl-2,3-dihydro-1H-benzoimidazol-2-yl)phenyl dimethy lamine (*N*-DMBI) to finely mediate the acceptor polarity in the donor-dilute devices based on the benchmark poly[[4,8-bis[5-(2-ethylhexyl)-4-fluoro-2thienyl]benzo[1,2-b:4,5-b′]dithiophene-2,6-diyl]-2,5-thiophene diyl[5,7-bis(2-ethylhexyl)-4,8-dioxo-4H,8H-benzo[1,2c:4,5c′]dithiophene-1,3-diyl]-2,5-thiophenediyl] (PM6):2,2′-((2Z,2′Z)-((12,13-bis(2-ethylhexyl)-3,9-diundecyl-12,13-dihy dro-[1,2,5]thiadiazolo[3,4-e]thieno[2′,3′:4′,5′]thieno[2′,3′:4,5]pyrrolo[3,2-g]thieno[2′,3′:4,5]thieno[3,2-b]indole-2,10-diyl)bis(methanylylidene))bis(5,6-difluoro-3-oxo-2,3-dihydro-1*H*-indene-2,1-diylidene))dimalononitrile (Y6) blends, where the more intra-connective donor phases were established with the concurrent suppression of the D/A intermixing and amelioration of phase purity [37]. Thirdly, while the layer-by-layer pseudo-planar heterojunction [22] and the molecular doping strategy [37] ensured a certain degree of phase purity, the accompanied reduction of D/A interfaces can cause the excitons generated by non-fullerene acceptors (NFAs) to recombine within the acceptor phases prior to migration towards the interfaces [38–40], awaiting to be resolved.

To address the last issue, this study as proof-of-concept selected the paradigm PM6:2,2′-((2Z,2′Z)((3,9-bis(2-butyloctyl)-12,13-bis(2-ethylhexyl)-12,13dihydro[1,2,5]thiadiazolo[3,4e]thieno[2′′,3′′:4′,5′]thieno[2′,3′:4,5]pyrrolo[3,2g]thieno[2′,3′:4,5]thieno[3,2b]indole-2,10-diyl)-bis(methaneylylidene))-bis-(5,6-difluoro-3-oxo-2,3-dihydro-1Hindene-2,1-diylidene))dimalononitrile (L8-BO) blends to prepare donor-diluted photovoltaic devices while using *N*-DMBI to optimize the acceptor-phase purity. In particular, we incorporated a polymer acceptor, poly(2,2′-((2Z,2′Z)-((12,13-bis(2-octyldodecyl)-3,9-diundecyl-12,13-dihydro[1,2,5]thiadiazolo[3,4e]thieno[2′,3′′:4′,5′]thieno[2′,3′:4,5]pyrrolo[3,2-g]thieno[2′,3′:4,5]thieno[3,2-b]-indole-2,10-diyl)bis(methanylylidene))bis(5-methyl-3-oxo-2,3-dihydro-1H-indene-2,1-diylidene))dimalononitrile-co-2,5-thiophene) (PYIT), as a third-component by utilizing the energy level difference between L8-BO and PYIT to promote exciton dissociation within the acceptor phases, thereby reducing dependences on the D/A interfaces. Notably, given a lower binding energy (E_b) of PYIT, its incorporation into the L8-BO system reduces E_b of the acceptors, which aids in the dissociation of photogenerated excitons within the acceptor phases and thereby enhances the exciton dissociation efficiency. Remarkably, PYIT can form entangled dual-acceptors with L8-BO, which reinforces intermolecular delocalization of excitons to prolong exciton lifetime, thereby increasing the probability of exciton dissociation. Consequently, the ternary donor-dilute PM6:L8-BO:PYIT-based semitransparent devices achieved an impressive PCE of 13.49%, with concurrently increased J_{SC} (22.47 mA cm^{-2}) and fill factor (FF = 0.70) as well as little changed open circuit voltage (V_{OC}). When introducing recently well-developed [2-(9H-carbazol-9-yl)ethyl]phosphonic acid (2PACz) as a hole-transporting layer (HTL), the device attained a record high LUE of 4.07% without any intricate processing techniques. By further adding TeO_2 as an antireflection coating (ARC) and replacing PM6 with PTB7-Th to display narrower optical bands, the AVT and LUE were synergistically boosted up to 54.27% and 5.63%, respectively. Our research explores the potential within existing photovoltaic material systems, providing a practical and scalable path to deploy semitransparent solar cells.

2. Experimental

2.1. Materials

PM6, PYIT, and L8-BO were purchased from Derthon Optoelectronics Materials Science Technology Co., Ltd. (China). *N*-DMBI was purchased from Sigma-Aldrich. All the materials were used as received without further purification.

2.2. Film morphology

For atomic force microscopy (AFM) imaging, the samples of PM6(30 wt%):PYIT(*x* = 0, 15, 25, 35, 45, 55, and 70 wt%):L8-BO (70–*x* wt%):*N*-DMBI(0.005 wt%) were prepared on the Si substrate following the same procedures as that applied for the deposition of device active layers, and the measurement was performed using NX10 microscope from Park Systems Co. Ltd. in the tapping mode. Transmission electron microscopy (TEM) images were captured by the equipment of JEOL JEM-F200. For the grazing incidence wide-angle X-ray scattering (GIWAXS) measurement, samples were drop-casted on the Si substrate from the blend solutions, and the two-dimensional (2D) diffraction patterns were acquired by beamline BL03HB at SSRF with an X-ray source of 10 keV and an incident angle of 0.2°. For grazing incidence small-angle X-ray scattering (GISAXS) measurements, samples were spin-casted on the Si substrate from the neat solutions. The 2D diffraction patterns were acquired by beamline BL16B1 at SSRF under an X-ray source of 10 keV and at an incident angle of 0.2°. The one-dimensional (1D) GISAXS profiles were extracted from Fit2D software and fitted on the basis of Fractal models by the software SASView (Version 5.0.4).

2.3. Optical spectra

Steady-state absorption spectra and photoluminescence (PL) spectra were measured by ultraviolet-visible (UV-vis) spectrometer of Agilent 8453 (Agilent Technologies Inc.) and equipment of FLS1000, respectively. Time-resolved photoluminescence (TRPL) spectra were measured by SpexFluorolog 1681 spectrofluorometer with the excitation wavelength of 800 nm. The TRPL spectra were fitted with the biexponential function of $I = I_0 + A_1 e^{-t/\tau_1} + A_2 e^{-t/\tau_2}$, the average exciton lifetime is calculated as $\tau_{avg} = \frac{A_1\tau_1 + A_2\tau_2}{A_1 + A_2}$, and the contributions of the fast and slow processes are evaluated by $f_i = \frac{A_i/\tau_i}{A_1/\tau_1 + A_2/\tau_2}$.

2.4. Transient absorption spectroscopy (TAS) methods

TAS measurements were performed on laser-based pump–probe spectroscopy. The laser pulses (400 and 800 nm, 40 fs pulse duration, and 2 kHz repetition rate) were generated by a femtosecond oscillator (Mai Tai SP, Spectra-Physics). For probing, a broad supercontinuum spectrum was produced by passing the laser through a thin sapphire crystal. The resulting beam was then split by a beam splitter into a probe pulse and a reference pulse. Both pulses were dispersed in a spectrograph and detected using a diode array (Pascher Instruments). The excitation fluence for the measurement was kept low as 1012 phonon/cm^2/pulse. In addition, global singular value decomposition (SVD) analysis was performed using the Glotaran software package (https://glotaran.org). This method combines a kinetic model with spectral components to construct a spectro-temporal model, providing a concise description of the system dynamics by estimating parameters such as rate constants and spectral features. Unlike conventional single-wavelength analysis, this unified, separable nonlinear model simultaneously accounts for all measurements across multiple independent variables.

2.5. In-situ UV-vis measurement

In-situ fast response UV-vis absorption spectroscopy measurements were obtained on a multi-spectrometer (DU-300, Shaanxi Puguang Weishi Co. Ltd.). According to the preparation process of the devices, the active layer materials dissolved in chloroform solution were spin-coated on clean quartz flakes. In this process, the in-situ UV-vis absorption spectra were obtained on a multi-spectrometer. The sampling intervals and integration times were set as 1 and 10 ms, respectively.

2.6. Device fabrication and measurement

Indium tin oxide (ITO)-coated substrates (15 Ω sq^{-1}) were ultrasonically washed with detergent, deionized water, acetone, and isopropanol in sequence for 25 min each step. After drying with argon flux, the substrates were treated with UV-ozone for 15 min. The solar cells were fabricated in the architecture of ITO/PEDOT:PSS/PM6:PYIT:L8-BO:*N*-DMBI(0.005 wt%)/PDINN/Ag. The PEDOT:PSS aqueous solution was spin-coated on precleaned ITO-coated glass at 4000 r min^{-1} for 30 s, and subsequently baked at 150 °C for 20 min in air to give a thin film with a thickness of ~30 nm. A blend of the PM6 donor and PYIT/L8-BO acceptor was dissolved in chloroform ($CHCl_3$) with a total concentration of 15 mg mL^{-1} for 4 h. To deposit active layers, the substrates were then transferred into an argon-filled glovebox, and the solutions of PM6(30 wt%):PYIT(*x* = 0, 15, 25, 35, 45, 55, and 70 wt%):L8-BO (70–*x* wt%):*N*-DMBI(0.005 wt%) were spin-coated onto the rotating substrate at 3000 r min^{-1}, followed by the thermal annealing at 85 °C for 10 min. Then methanol solution of PDINN at a concentration of 1.0 mg mL^{-1} was deposited atop the active layer at 3000 r min^{-1} for 30 s to afford a PDINN electron transport layer. Finally, the top electrode of 120 nm (for opaque devices) or 20 nm (for semi-transparent devices) Ag thin films was thermally evaporated onto the samples at a base pressure of 10^{-4} Pa, which were patterned with a shadow mask. Unencapsulated solar cells with an active area of 0.04 cm^2 were tested under AM 1.5G irradiation (Newport-Oriel) in air, and the current density-voltage (*J-V*) curves were recorded using a Keithley 2400 source meter, with light intensity determined by a 2 cm × 2 cm standardized monocrystalline silicon cell. *J-V* curves were scanned with a voltage increment of 0.02 V and a dwell time of 20 ms. The external quantum efficiency (EQE) profiles were measured using the QE-R setup designed by Enli Technology Co., Ltd. with a 500 W xenon lamp.

2.7. Space-charge-limited current (SCLC) characterization

Electron- and hole-only devices were fabricated with configurations of ITO/ZnO/active layer/PDINN/Ag and ITO/PEDOT:PSS/active layer/MoO_3/Ag. *J-V* curves were measured in the dark with a Keithley 2400 source meter. Charge mobilities (μ) were determined from linear fittings of the semi-log plot of SCLC curves according to the Mott-Gurney model of $J = \frac{9}{8}\mu\varepsilon_r\varepsilon_0\frac{V^2}{d^3}$, where *J* is the current density, *V* is the applied voltage, ε_r is the relative dielectric constant of 3 for organic semiconductors, ε_0 is the vacuum permittivity of 8.8542 × 10^{-12} F m^{-1}, and *d* is the active layer thickness measured by a step-profilometer.

3. Results and discussion

3.1. Unveiling inefficient exciton dissociation in donor-dilute ST-OSCs

This study investigates those best-known organic/polymeric photovoltaic materials, PM6 donor and L8-BO/PYIT acceptors, for constructing highly efficient ST-OSCs, with the corresponding chemical structures and energy diagrams displayed in Fig. 1(a). Note that both the highest occupied molecular orbital (HOMO) and lowest unoccupied molecular orbital (LUMO) energy levels of PYIT (denoted as E_{HOMO} and E_{LUMO}, respectively, for brevity) are higher than those of L8-BO, thereby establishing a cascade alignment for effective charge transfer between two acceptors. Steady-state PL spectra (Fig. 1b) were characterized to probe exciton dissociation and charge transfer behaviors in the blend films. L8-BO displays a prime optical absorption band at a wavelength of 800 nm (Fig. S1), which was selectively photo-excited and yielded a characteristic emission peak at 917 nm (Fig. S2). Likewise, in the binary PM6(100–*x* wt%):L8-BO(*x* wt%) blend film (Fig. 1b-i) when photo-excited by 800 nm, the fluorescence of L8-BO is progressively enhanced with the decreasing PM6 content. This suggests a declining exciton dissociation efficiency due to the reduced D/A interfaces to leave more excitons to undergo radiative recombination [41,42]. Such an issue was also identified by our previous work in donor-diluted ST-OSCs, which found a PM6 donor content of 30 wt% in the blend to be an optimal ratio for reaching a fine trade-off between AVT and PCE in semi-transparent devices. On this basis, we attempted to add a polymeric acceptor PYIT to facilitate exciton dissociation. By increasing the PYIT content from 0 to 70 wt% into the dilute PM6(30 wt%):L8-BO blend, it is unveiled that at a low content of 15 wt% PYIT in the blend film, the PL quenching of the dual L8-BO/PYIT acceptors was the most pronounced (Fig. 1b-ii). We speculate that an appropriately small amount of PYIT can be readily intercalated into the amorphous regions of L8-BO to enlarge interfaces between two acceptors (as discussed in the following section) and augment exciton delocal-

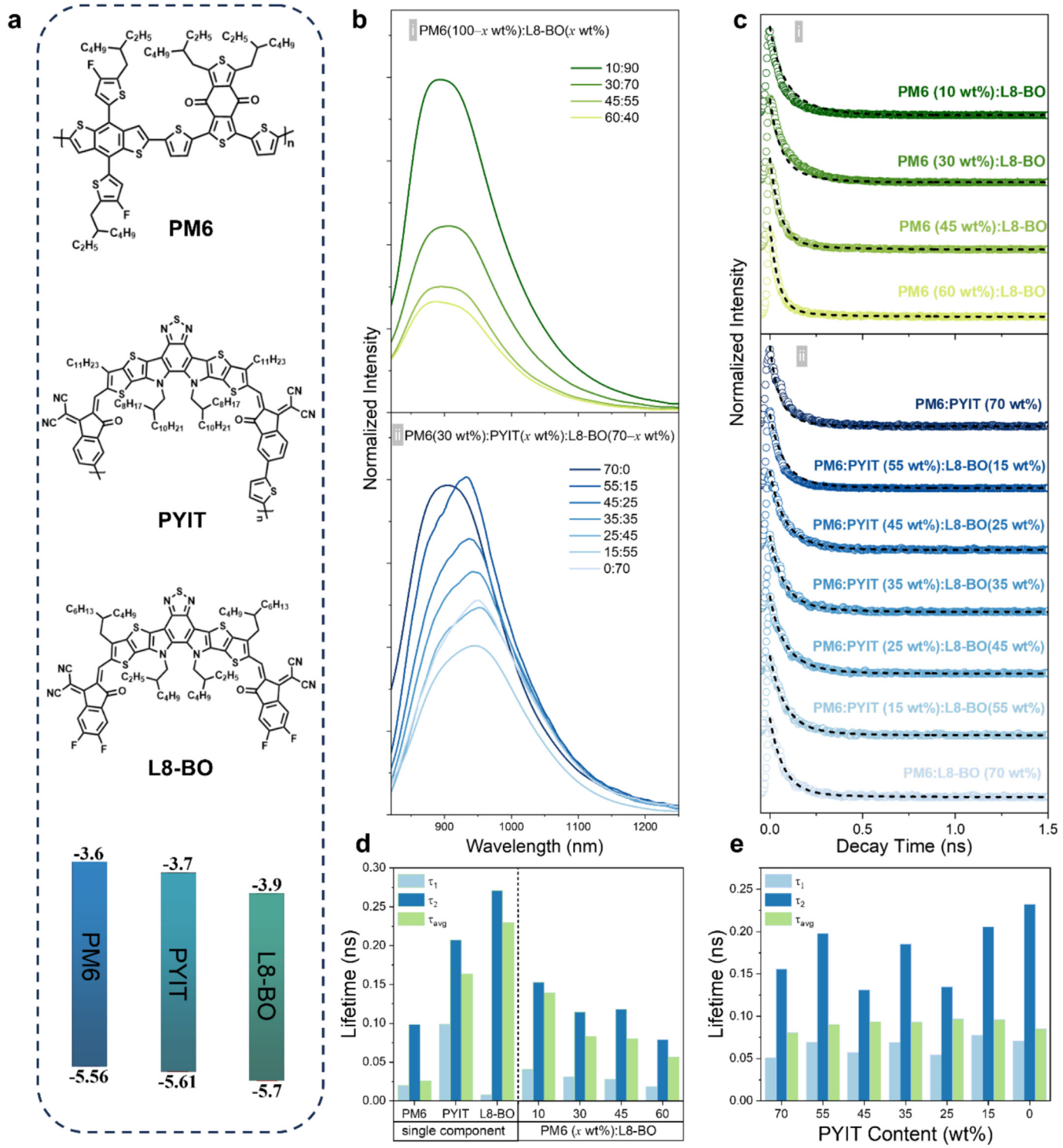

Fig. 1. Fluorescence quenching in multi-component active layers in ST-OSCs. (a) Molecular structures and energy diagrams of PM6 donor and PYIT/L8-BO acceptor. (b) Steady-state PL spectra of the *N*-DMBI-doped thin films including (i) PM6(10, 30, 45, and 60 wt%):L8-BO binary blends and (ii) PM6(30 wt%):PYIT(*x* wt%):L8-BO(70–*x* wt%) ternary blends at 800 nm excitation. (c) TRPL decay profiles of the binary and ternary thin films measured under 850 nm photo-excitation and (d and e) their exciton lifetimes, respectively.

ization or even dissociation, given their heterojunction energy alignment as shown in Fig. 1(a). This alleviates the dependence on the D/A interfaces while reinforcing charge transfer and extraction.

TRPL decays were further acquired to examine the effect of the added PYIT on the exciton dissociation and recombination processes (Fig. 1c–e). All the TRPL kinetics can be well-fitted by using a biexponential function, consisting of two components τ_1 and τ_2, which correspond to the processes of fast nonradiative recombination/charge transfer and slow radiative/trap-assisted recombination, respectively. The contributions of each process can be assessed by the weighted fractions (f_1 and f_2) of τ_1 and τ_2

(Fig. S3). In the PM6:L8-BO blend film, a gradual increase in the PM6 ratio from 10 to 45 wt% can moderately increase the volume fraction of the D/A intermixing, thus accelerating interfacial exciton dissociation to quench PL emission. As a result, τ_1 and τ_2 values are slightly shortened from 41 and 153 ps to 28 and 118 ps, respectively, yielding a remarkable drop of average lifetime (τ_{avg}) from 139 to 80 ps (Fig. 1c-i and d). These results suggest that with the reduction of the donor content, the excitons in the acceptor phase cannot dissociate through the D/A interfaces, leading to a more pronounced exciton recombination and an overall longer PL lifetime. Based on our previous study and the comparison with literature reports, we continued to choose an optimal PM6 content of 30 wt% as proof-of-concept in this work to construct ST-OSCs. Owing to the reduction in donor content, however, the free hole carriers dissociated from excitons in NFAs remain to be ineffectively transported and mostly left within the acceptor phase to undergo bimolecular recombination with free electrons. Therefore, we incorporated PYIT as a third component to the binary blend, aiming to mitigate such charge recombination within L8-BO acceptor.

When adding an optimal 15 wt% PYIT to the PM6(30 wt%):L8-BO blend, despite the remarkably enhanced PL quenching compared to the binary film as shown in Fig. 1(b-ii), we find an elevation of f_2 from 2.89% to 6.06% and hence an extension of τ_{avg} from 83 to 96 ps (Fig. 1c-ii and e). This is mainly caused by the PYIT-induced effect that the interfacial charge transfer is likely to occur at much shorter time-scales than the instrumental response function of the TRPL setup, which will be further validated in later transient absorption measurements. On the other hand, the prolonged PL lifetime at longer time-scales is presumably due to the similar chemical structures and aligned energy levels of PYIT and L8-BO, which facilitate the formation of an entangled acceptor phase to strengthen exciton delocalization. This is further corroborated by lower E_b of the dual L8-BO:PYIT acceptor phases (106.20 meV) than that of neat L8-BO (170.19 meV), as measured and fitted by temperature-dependent PL spectra in Fig. S4. Lower E_b will promote the spontaneous dissociation of photogenerated excitons within the acceptor phase to free carriers, which usually exhibit longer lifetimes than excitons [43–45].

3.2. Optimizing dual-acceptor composition in donor-dilute ST-OSCs

We next illustrated how the addition of PYIT favorably affects exciton dissociation and enhances PCEs in donor-dilute ST-OSCs. Firstly, we constructed opaque devices based on ITO/PEDOT:PSS/PM6:L8-BO:*N*-DMBI(0.005 wt%)/PDINN/Ag (120 nm), and the *J-V* curves with the corresponding photovoltaic parameters of the devices are shown in Fig. S5 and summarized in Table S1, respectively. When the content of PM6 donor is gradually reduced from 45 to 30 and 10 wt%, J_{SC} decreases from 25.09 to 21.38 and 20.79 mA cm^{-2}, respectively, while V_{OC} remains unchanged. This can be ascribed to the reduction of the D/A interfaces, which leads to inefficient exciton dissociation. Subsequently, we introduced a third-component PYIT and fabricated a series of devices based on ternary ITO/PEDOT:PSS/PM6:PYIT(x wt%):L8-BO(70–x wt%):*N*-DMBI(0.005 wt%)/PDINN/Ag devices, for which Ag electrode thicknesses of 100 and 20 nm were used for opaque and semitransparent cells, respectively. The *J-V* curves of opaque devices and the corresponding photovoltaic data are shown in Fig. S6 and Table S2. After adding PYIT, the V_{OC} gradually increases from 0.84 to 0.94 V as a function of PYIT content, thanks to a larger disparity between the E_{LUMO} of PYIT and the E_{HOMO} of PM6, along with the smaller exciton E_b of PYIT, which reduces the energy required for exciton dissociation and thus decreases the loss in V_{OC}. In contrast, J_{SC} exhibits an opposite trend; that is, when the content of PYIT increases from 15 to 70 wt%, J_{SC} gradually decreases from 23.33 to 20.57 mA cm^{-2}. This is attributed to PYIT being a polymer with a lower crystallinity compared to L8-BO, resulting in a larger number of defects in its amorphous regions, which leads to significant non-radiative recombination.

The *J-V* curves and corresponding photovoltaic data of ST-OSCs are shown in Fig. 2(a) and Table S3, respectively. The EQE spectra are displayed in Fig. S7, from which the integrated J_{SC} coincide with the measured values with an error of less than 5%. In comparison to the opaque devices, we find that reducing the thickness of the Ag electrode from 100 to 20 nm significantly decreases J_{SC} from 23.59 to 22.47 mA cm^{-2} at an optimal ratio of PYIT (15 wt%). This results in a reduction of PCE from 14.54% to 13.49% while holding minimal effect on V_{OC} (0.88–0.86) and FF (~0.70). This phenomenon is primarily due to the reduced charge extraction capability and the increased number of surface defects that exacerbate defect-assisted recombination as the Ag electrode becomes thinner.

We then evaluated the optical transparency of the PM6(30 wt%):PYIT(x wt%):L8-BO(70–x wt%) blends and devices. A photograph of schematic device architecture is taken to visually illustrate the device transparency as shown in Fig. 2(b). Fig. 2(c, d) presents the optical absorption and transmission spectra of the active layers with varied acceptor ratios and the corresponding semitransparent solar cells. We found such an intriguing trend that an increase in the PYIT content led to a higher CRI, thus achieving a notable value of 80.66 in the binary film PM6:PYIT. Additionally, an increase in the L8-BO content results in a higher AVT, with the binary PM6:L8-BO(70 wt%) devices achieving an impressive AVT of 27.22%. This phenomenon might be caused by the red-shifted absorption band of L8-BO relative to that of PYIT, thereby weakening absorption in the visible light region. Despite a slight decrease in AVT to 26.39%, the LUE reaches a peak of 3.56% while the CRI stands at 68.80.

To reinforce device performance, we replaced the conventional PEDOT:PSS HTL with a recently developed self-assembled layer, 2PACz. In comparison, 2PACz displays weaker visible light absorption, and meanwhile it increases the work function of ITO, thus aiding in hole extraction [46]. Through the interaction of molecular dipole moments and charge transfer characteristics with the electrode surface, the 2PACz HTL optimizes the energy level alignment, ultimately leading to a slight enhancement in V_{OC} and J_{SC} from 0.86 V and 22.47 mA cm^{-2} to 0.88 V and 22.70 mA cm^{-2}, respectively (Fig. 2e). To be more meaningful, Fig. 2(f) compares our data with the reported results of representative donor dilute ST-OSCs without any other complicated processing (the detailed data are listed in Table S4), which marks the highest LUE value in this study.

Based on it, we utilized the PTB7-Th donor with a narrower bandgap to substitute PM6 and high refractive index TeO_2 as an antireflective layer to further increase AVT [47]. While this resulted in a marginal reduction in PCE with V_{OC}, J_{SC}, and FF of 0.74 V, 19.80 mA cm^{-2}, 0.71, respectively, the AVT was improved significantly to 54.27%, with the LUE reaching a superior value of 5.63%. We also compared our results with previously reported LUE values exceeding 5% in the literature, which further confirms that the performance we obtained is highly competitive (Fig. 2f and the detailed data are listed in Table S5). All these device data are visually summarized in Fig. 2(g), with reliability corroborated by the corresponding transmission and EQE profiles provided in Fig. S8.

3.3. Characterizing bi-acceptor networks in donor-dilute ST-OSCs

To comprehend the effects of PYIT addition on film morphologies in donor-dilute ST-OSCs, we conducted a systematic characterization of surface topography, phase-segregation, molecular packings, and phase purity of the active layers. Tapping-mode

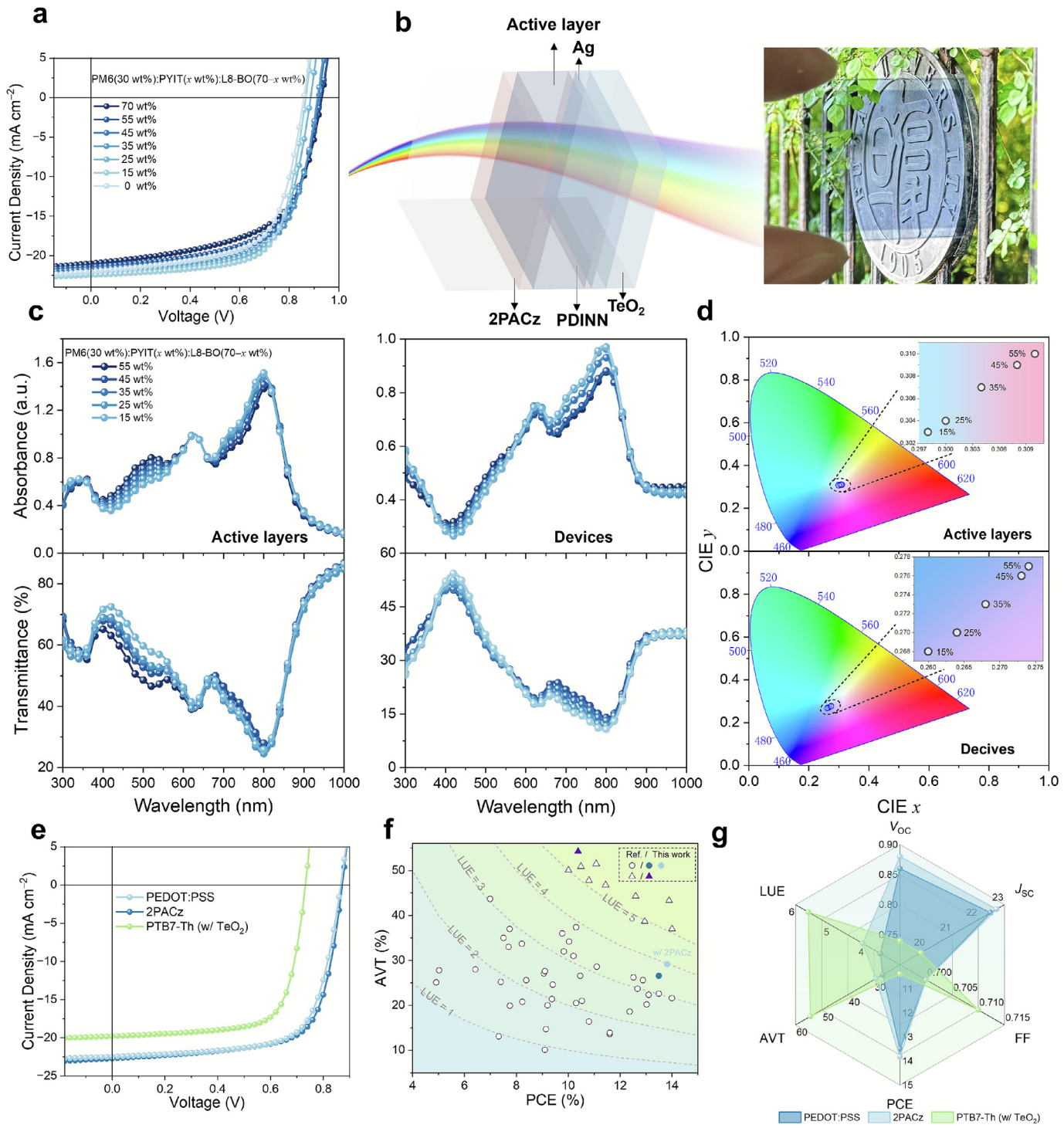

Fig. 2. Photovoltaic performance and visible transparency. (a) *J-V* curves of the ST-OSCs based on 20 nm-thick Ag electrode and PM6(30 wt%):PYIT(x = 0, 15, 25, 35, 45, 55, and 70 wt%):L8-BO(70–x wt%) blends. For each composition, 15 replicates were made and measured in the same batch to demonstrate experimental reproducibility. (b) A schematic device of ST-OSCs and a photograph of the champion ST-OSCs based on the optimal active layers of PM6/PTB7-Th (30 wt%):PYIT(15 wt%):L8-BO(55 wt%). (c) Optical absorption and transmittance spectra and (d) the calculated coordinates in chromaticity diagrams of PM6(30 wt%):PYIT(x = 15, 25, 35, 45, and 55 wt%):L8-BO(70–x wt%)-based active layers and the corresponding semi-transparent devices with a 20 nm-thin Ag electrode. (e) *J-V* curves of ST-OSCs via further optimization by 2PACz and TeO_2 on the champion devices. (f) Comparison of AVT and PCE values in this work with those reported in literature. (g) Statistical data profiles.

AFM (TP-AFM) topography images of the PM6:PYIT, PM6:PYIT(15 wt%):L8-BO(55 wt%), and PM6:L8-BO blend films were firstly acquired and shown in Fig. 3(a). The corresponding root-mean-square (RMS) surface roughness values are estimated to be 1.287, 2.420, and 3.355 nm, respectively. The highest RMS roughness of the PM6:L8-BO blend is presumably ascribable to the better crystallinity and over-aggregation of L8-BO. The addition of 15 wt% polymer PYIT, featuring the inherently flexible and amorphous structural characteristics, would inhibit the excessive aggregation of small-molecule L8-BO. This results in a smoother morphology of the active layer and a better interpenetrating network, thereby enhancing both J_{SC} and FF of the ternary devices.

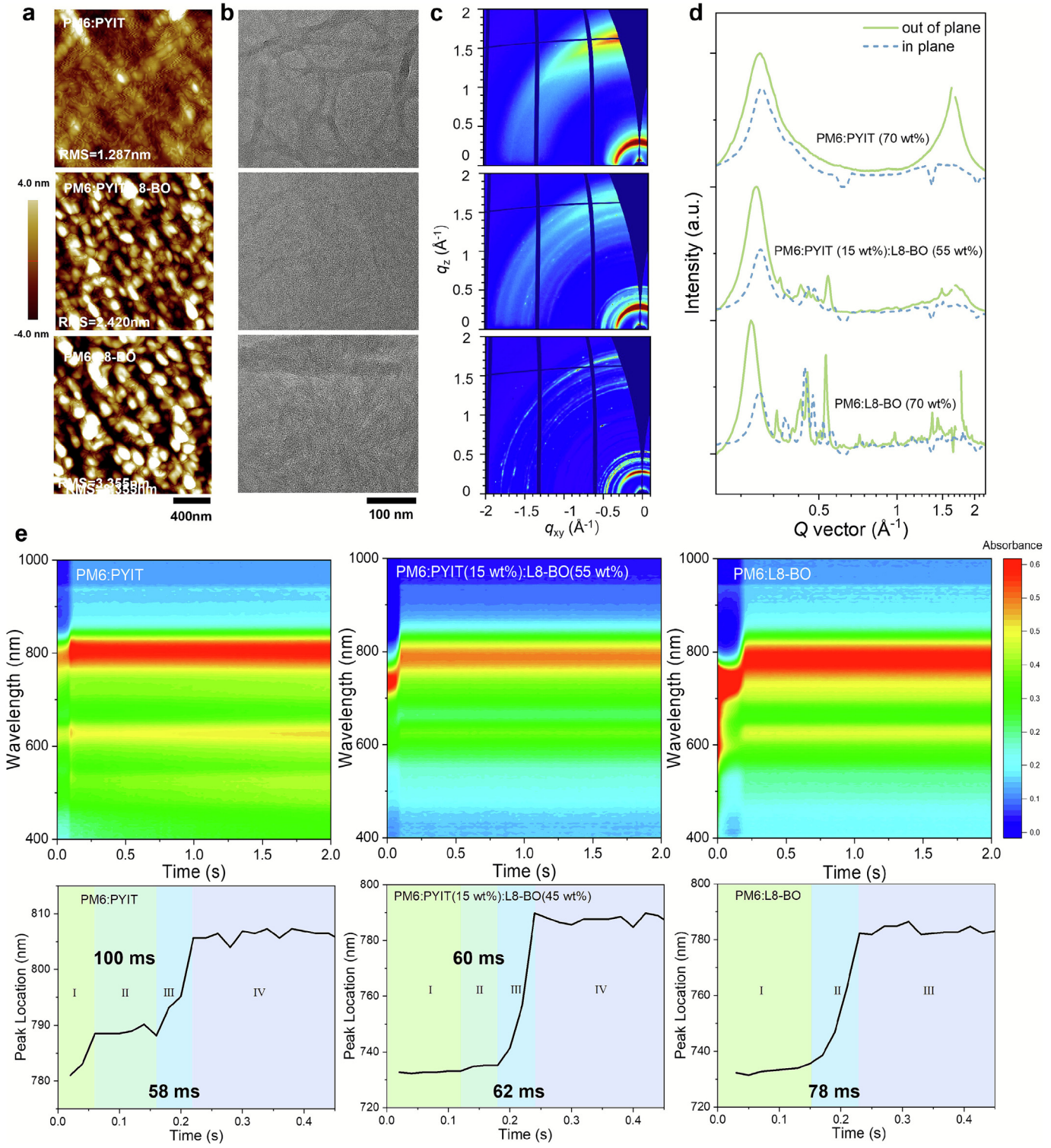

Fig. 3. Phase separation and active-layer morphology. (a) TP-AFM height images, (b) TEM images, (c) 2D GIWAXS patterns, and (d) 1D linecuts of PM6(30 wt%):PYIT(x = 0, 15, and 70 wt%):L8-BO(70–x wt%) active layers. (e) In-situ absorption spectra of the same active layer condensed from its chloroform solution, and the corresponding time evolution of peak location. Note that there is a significant overlap for the main peaks of PYIT and L8-BO.

Next, TEM measurement was performed to obtain the nanoscale phase-separation of the above-mentioned blend films. TEM images (Fig. 3b) visualize the nanoscale phase-separation of the blend films. Among them, the phase-segregation of the PM6:PYIT film is highly uneven, leading to an excessive number of defects that impede charge transport and result in a lower J_{SC}, as shown in Fig. 2(a). By contrast, the PM6:L8-BO film displays excessive aggregation of the acceptor, resulting in large-scale phase-separation that adversely affects charge separation and transport. Contrary to the above two, the PM6:PYIT:L8-BO blend film displays a

bi-continuous interpenetrating network morphology with appropriate nanoscale phase-separation, contributing to exciton dissociation and charge transport.

To in-depth characterize the entangled structure formed by L8-BO and PYIT acceptors, we conducted GISAXS measurements on their neat films. The corresponding patterns (Fig. S9a–c) were analyzed via Fractal model fitting (Fig. S9d–f), with parameters summarized in Table S6, to determine the crystalline domain sizes of the acceptors. It is unveiled that the domain size of the PYIT:L8-BO blend film is larger than that of the neat L8-BO film, that is, R_g = 79.2 nm versus 71.8 nm. This finding points to a high miscibility between PYIT and L8-BO, enabling PYIT to connect the isolated crystalline regions of L8-BO.

To probe intermolecular packings and orientations of the active layers, GIWAXS characterization was carried out. The 2D scattering patterns and cut-line profiles are provided in Fig. 3(c, d), and corresponding molecular packing parameters are shown in Table S7. The PM6:PYIT blend film displays lamellar stacking in the in-plane (IP) direction at 0.311 $Å^{-1}$ and π-π stacking peak in the out-of-plane (OOP) direction at 1.644 $Å^{-1}$ with a π-π distance of 3.82 Å. Conversely, the PM6:L8-BO blend film exhibits (100) diffraction peak at 0.303 $Å^{-1}$ in the IP direction and (010) diffraction peaks at 1.771 $Å^{-1}$ in the OOP direction, corresponding to a stacking distance of 3.53 Å. The crystalline coherence length (CCL) of π-stackings in the PM6:PYIT and PM6:L8-BO blends is calculated to be 23.58 and 55.92 Å, respectively, according to the Scherrer equation. It is seen that the crystallinity and compactness of molecular stackings in L8-BO are significantly greater than those in PYIT. The excessive amorphous regions in PYIT may lead to increased scattering and hence hinder charge transport and decrease electrical conductivity. In conjunction with the TP-AFM images, we can discern that L8-BO forms numerous isolated island-like crystalline regions. Such a lack of effective interconnectivity among these isolated regions restricts the migration pathways of charge carriers within the acceptor phase, thereby reducing charge transport efficiency. However, after incorporating 15 wt% PYIT in the OOP direction, the π-π stacking distance (3.68 Å) and CCL (24.30 Å) are obtained for the PM6:PYIT:L8-BO. This is attributed to the high degree of intermixing between PYIT and L8-BO, which helps to well connect isolated island-like crystalline regions of L8-BO, thereby forming a continuous network of the acceptor phase. This may, nevertheless, lead to a reduction in the short-range crystallinity of L8-BO yet promotes free migration of charge carriers within the acceptors, which reduces defect-assisted recombination and increases J_{SC}.

We further performed an in-depth study on how PYIT affected the crystallization and molecular arrangement of L8-BO by applying in-situ UV-vis absorption spectroscopy. The temporal progression of peak location of PM6:PYIT, PM6:PYIT:L8-BO, and PM6:L8-BO is presented in Fig. 3(e). It can be seen that during the film formation of the PM6:PYIT blend, there is a plateau lasting 100 ms, which can be explained as a precipitation process of PYIT, whose actual crystallization time is only 58 ms. In the case of the PM6:L8-BO blend, in contrast, their excellent miscibility makes it difficult to observe the precipitation of L8-BO. However, a relatively longer crystallization time of 78 ms is noticed. Upon the addition of 15 wt% PYIT, a precipitation process occurred more rapidly (60 ms), followed by a slower crystallization period (62 ms). This indicates that when L8-BO began to crystallize, PYIT already occupied some of the available space for crystal growth, which interfered with the crystallization of L8-BO by shortening crystallization and minimizing excessive aggregation.

Owing to the ameliorated film morphologies as analyzed above, we assessed the storage stability of the unencapsulated optimal semi-transparent ternary device in comparison with that of the binary device. The results shown in Fig. S10 are expected to demonstrate that the champion PM6:PYIT(15 wt%):L8-BO(55 wt%) donor-dilute device exhibits superior long-term storage in air by maintaining ~70% of initial efficiency in contrast to the binary counterparts, since the optimal phase-separated morphologies in ternary blend films prevent the degradation of charge transport pathways caused by uncontrolled component aggregation.

3.4. Probing excited-state lifetimes and dynamics in donor-dilute active layers

To gain deep insights into how the incorporation of PYIT impacts exciton separation and charge carrier transfer within the active layer, TAS was employed to track the excited-state dynamics of the PM6:PYIT, PM6:PYIT:L8-BO, and PM6:L8-BO blend films. Two wavelengths of 400 and 800 nm were utilized to selectively photo-excite PM6 and L8-BO/PYIT, respectively, thereby allowing us to elucidate the depopulation pathways of the donor excitons and the acceptor excitons. The obtained TAS 2D spectra (Fig. S11) were then subjected to SVD fitting, enabling a comprehensive analysis of each dynamic process after excitation, as shown in Fig. 4.

When pumped at 800 nm, where only PYIT can be excited, the TAS spectra of the blend films can all be decomposed into three components with identical spectral features, as illustrated in Fig. 4(a). The fastest components (green curves) with picoseconds lifetimes (1.7, 2.2, and 3.5 ps) display ground state bleach (GSB) signal at 825 nm, ascribed to the main absorption band of L8-BO/PYIT in ground state absorption spectra, suggesting the depopulation of excited charges in L8-BO/PYIT. The positive signals from 500 to 650 nm mirror the GSB of PM6, which can be assigned to the population of excited charges in PM6. These two concurrent features indicate the process of hole transfer from the L8-BO/PYIT acceptor to the PM6 donor. The slower component (light blue curves) with lifetimes of tens of picoseconds resembles the spectral feature of neat L8-BO/PYIT, which can be related to exciton-exciton annihilation within L8-BO/PYIT [48,49] based on the locations of the GSB (825 nm) and excited state absorption (ESA, 600 nm) signals, suggesting that the photogenerated excitons in non-fullerene acceptors lowered the effective exciton dissociation efficiency due to the donor dilution and the reduced D/A interface. The slowest components (dark blue curves, 2.4, 2.6, and 4.7 ns) featured both GSB signals at 625 and 825 nm, corresponding to the simultaneous depopulation of charge carriers in PM6 and L8-BO/PYIT. Therefore, this component can be attributed to the geminate electron-hole recombination at interfaces. The extracted dynamics processes can then be illustrated in Fig. 4(b–d).

When using 400 nm pump light to excite both PM6 and PYIT:L8-BO in the blend films, both electron and hole transfer pathways can be identified from the SVD fitting in Fig. 4(e–h). The TAS spectrum of PM6:PYIT can be fitted into two components with lifetimes of 9.3 ps (green curve) and 900 ps (dark blue curve), which can be assigned to the hole transfer from PYIT to PM6 and the interfacial geminate electron-hole recombination, respectively, identical to the case of 800 nm excitation. The PM6:PYIT:L8-BO and PM6:L8-BO samples both contain an additional component (light blue curve) with a PM6 GSB signal generated around 630 nm and a derivative feature (negative at shorter wavelengths and positive at longer wavelengths) centered at the maximum of the acceptor GSB band, as indicated by the dashed lines. This feature is hypothesized to be a mixture of positive mirroring of acceptor GSB bands and a blue shift of the absorption band of the acceptor ground state due to the photo-induced Stark effect [50]. Thus, this component should account for the concurrent charge carrier depopulation in donors and population in acceptor, i.e., the electron transfer from PM6 to L8-BO/PYIT. The absence of such an electron injection-related component in PM6:PYIT film can arise from the fast process that reaches the response function of the instrument (100–200 fs).

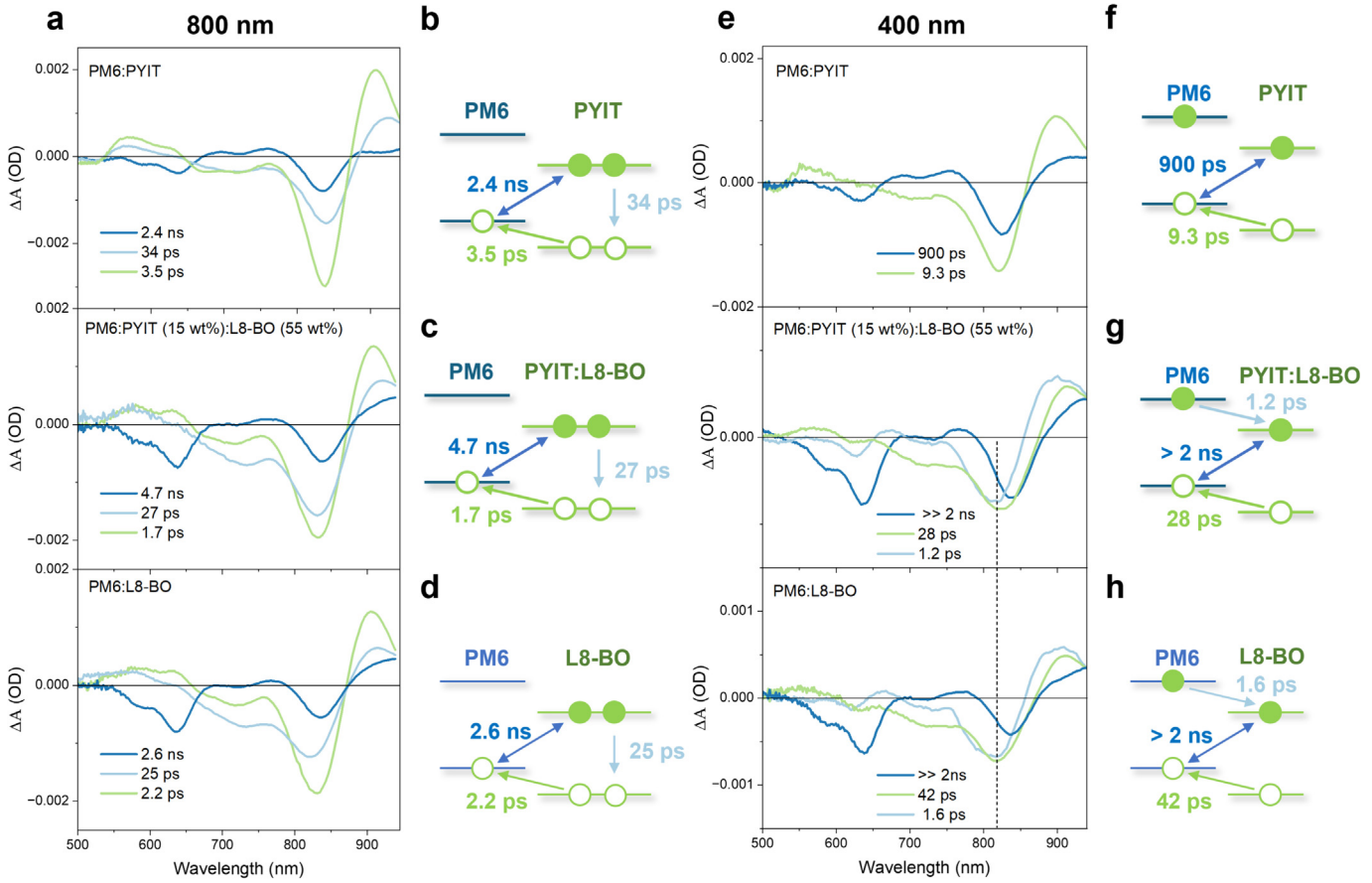

Fig. 4. Exciton and carrier dynamics. (a) Single-value-decomposition analysis for the TAS of the PM6(30 wt%):PYIT(x = 70, 15, and 0 wt%):L8-BO(70–x wt%) active layers measured under 800 nm photo-excitations. (b–d) Corresponding schematics and times taken for each process. (e) Single-value-decomposition analysis for the TAS of the PM6 (30 wt%):PYIT(x = 70, 15, and 0 wt%):L8-BO(70–x wt%) active layers measured under 400 nm photo-excitations. (f–h) Corresponding schematics and times taken for each process.

A comparison of the extracted charge carrier transfer and recombination dynamics from these two excitation scenarios is summarized in Fig. 4(b–d and f–h), respectively. We can conclude that incorporating 15 wt% of PYIT into the PM6:L8-BO blend accelerates both hole and electron transfer processes. This enhancement can be attributed to the formation of an entangled dual-acceptor morphology—a consequence of the interaction between L8-BO and PYIT. This interaction leads to the creation of greater delocalization space through spatial overlap or interaction. The enhanced electronic coupling between different acceptors further improves electron mobility, thus reducing charge carrier recombination during transport. Furthermore, the splitting of PYIT/L8-BO energy levels facilitates dissociation of excitons upon photo-generation within acceptor phases, as also manifested by the above-mentioned long PL lifetime and low E_b values, the latter of which would help lower the probability of exciton-exciton annihilation—a critical channel for the photocurrent loss. This, in turn, results in more dominant and stabilized charge-separated states. Based on the previous AFM and TEM images, polymeric PYIT, being more flexible and amorphous than small-molecule L8-BO, suppressed excessive aggregation of L8-BO, resulting in a smoother active layer morphology, while ameliorating the orientation and continuity of the acceptor phase. Due to the lower miscibility of PYIT and PM6, on the other hand, a certain degree of phase-separation was achieved, which further reduced the probability of bimolecular recombination [40].

3.5. Unveiling charge transport mechanisms in donor-dilute ST-OSCs

Given that the incorporation of 15 wt% PYIT into blend films could mitigate non-radiative recombination and facilitate charge transport as discussed in previous sections, we strove to further unravel charge recombination and transport mechanisms at the device level by light-dependent J-V and SCLC measurements. To unveil the charge recombination mechanism in working devices, we analyzed the J-V curves of the opaque devices based on ternary PM6(30 wt%):PYIT(x = 0, 15, 25, 35, 45, 55, and 70 wt%):L8-BO(70 –x wt%) active layers under different light intensities. The formulas of $V_{OC} \propto k_B T\omega \ln(P_{in})/q$ and $J_{SC} \propto (P_{in})^{\alpha}$ represent the power-law relationships between V_{OC}, J_{SC} and the light intensity (P_{in}), respectively [51]. In these two formulas, ω and α are used to describe the open-circuit trap-assisted recombination and the short-circuit bimolecular recombination, respectively [52]. As shown in Fig. S12(a), for the PM6:L8-BO device, ω is calculated to be 1.385, indicative of severe trap-assisted recombination, which is ascribed to defect sites at the interfaces due to the weak bonding between L8-BO crystals. Remarkably, the incorporation of a minor quantity (15 wt%) of PYIT effectively fills these trap states, with ω dropping to 1.316, suggesting the effective suppression of trap-assisted recombination. For the bimolecular recombination, although devices with different PYIT ratios show similar α, the favorable effects of the PYIT addition on inhibiting bimolecular recombination could still be observed. Specifically, α shows an increasing then decreasing trend and reaches 0.990 at a PYIT ratio

of 15 wt%. When the content of PYIT continues to increase, their α values deviate from 1, manifesting the progressively increasing bimolecular recombination. This is attributed to the relatively amorphous domains of PYIT, as discussed previously, which is unfavorable for charge transport and extraction, ultimately leading to the collision of dissociated electrons and holes under the Coulombic effect. In short, the addition of 15 wt% PYIT can not only fill trap states within L8-BO but also form energy level offsets with L8-BO to promote charge transport, thereby minimizing non-radiative recombination of carriers in devices.

To quantitatively characterize charge transport properties, SCLC measurements were conducted under single-carrier devices. The SCLC curves and the carrier mobilities calculated by using the Mott-Gurney model are shown in Figs. S12(b) and S13, respectively. Due to the diluted donor content (30 wt%), both electron (μ_e) and hole (μ_h) mobilities exhibit relatively low values. In the case of the PM6:L8-BO device, μ_e and μ_h are determined to be 1.28×10^{-4} and 1.00×10^{-4} cm^2 V^{-1} s^{-1}, respectively, yielding μ_e/μ_h = 1.28. Interestingly, as the PYIT contents gradually increase, μ_e decreases first and then increases, while μ_h displays the opposite trend. The reason for the initial decrease in μ_e is that a small amount of PYIT weakens the crystallinity of L8-BO and disrupts the acceptor network for electron transport. The subsequent increase in μ_e could be caused by the fact that PYIT exhibits a lower E_b, allowing excitons to dissociate more readily into electrons and holes within the acceptor phases. Therefore, the device containing 15 wt% PYIT demonstrates a more balanced μ_e (1.22×10^{-4} cm^2 V^{-1} s^{-1}) and μ_h (1.11×10^{-4} cm^2 V^{-1} s^{-1}), contributing to both higher J_{SC} and FF among others.

4. Conclusions

In closing, we demonstrated that the incorporation of a polymeric PYIT acceptor into donor-dilute PM6:L8-BO blends effectively resolved the critical challenges of inefficient exciton dissociation and severe charge recombination in ST-OSCs. Morphological and spectroscopic analyses revealed that by forming entangled dual-acceptor phases with L8-BO, PYIT suppressed excessive aggregation of L8-BO, promoted bi-continuous phase-segregation, and elevated charge carrier mobility. Consequently, intermolecular exciton delocalization is strengthened and exciton lifetimes are prolonged from 83 to 96 ps, leading to a best PCE of 13.49% in devices. Further transparency enhancements were achieved by integrating a 2PACz HTL, a TeO_2 antireflective coating, and a substitution with PTB7-Th donor, all of which collectively resulted in the highest AVT of 54.27% and a champion LUE of 5.63%. These findings prioritize a dual-acceptor phase-engineering strategy in leveraging efficiency and transparency for ST-OSCs, paving the way for their practical deployment in building-integrated photovoltaics.

CRediT authorship contribution statement

Xiaoxiao Zhang: Conceptualization, Investigation, Writing – original draft, Writing – review & editing. **Zhiyuan Wu:** Investigation, Writing – review & editing. **Jiaqi Xie:** Investigation, Writing – review & editing. **Weihua Lin:** Investigation. **Kaibo Zheng:** Supervision, Writing – original draft, Writing – review & editing. **Ziqi Liang:** Conceptualization, Investigation, Supervision, Writing – original draft, Writing – review & editing.

Declaration of competing interest

The authors declare that they have no known competing financial interests or personal relationships that could have appeared to influence the work reported in this paper.

Acknowledgments

This work was financially supported by the National Natural Science Foundation of China (NSFC) under grant No. 22375050 and the Shanghai Leading Talent Program of Eastern Talent Plan. K.Z. acknowledges the research grants from the Swedish Research Council (No. 2021-05319). We thank BL03HB beamlines at Shanghai Synchrotron Radiation facility (SSRF) for the GIWAXS beamtimes. We thank Xiaoyue Hu from the State Key Laboratory of Molecular Engineering of Polymers at Fudan University for fluorescence measurements, as well as SCI-GO (https://www.sci-go.com) for TEM testing. We also thank Prof. Xiaosheng Fang for the support of thermal evaporation of TeO_2.

Appendix A. Supplementary material

Supplementary data to this article can be found online at https://doi.org/10.1016/j.jechem.2025.11.015.

References

[1] F. Cheng, Y. Cui, F. Ding, Z. Chen, Q. Xie, X. Xia, P. Zhu, X. Lu, H. Zhu, X. Liao, Y. Chen, Adv. Mater. 35 (2023) 2300820.
[2] Y. Cho, T.H. Lee, S. Jeong, S.Y. Park, B. Lee, J.Y. Kim, ACS Appl. Energy Mater. 3 (2020) 7689–7698.
[3] D. Corzo, E. Bihar, E.B. Alexandre, D. Rosas-Villalva, D. Baran, Adv. Funct. Mater. 31 (2020) 2005763.
[4] E. Mazzolini, R.A. Pacalaj, Y. Fu, B.R. Patil, R. Patidar, X. Lu, T.M. Watson, J.R. Durrant, Z. Li, N. Gasparini, Adv. Sci. 11 (2024) 2402637.
[5] X. Xiong, S. Wan, B. Hu, Y. Li, Y. Ma, G. Lu, H. Fu, Q. Zheng, Adv. Energy Mater. 14 (2024) 2401816.
[6] J. Fu, Q. Yang, P. Huang, S. Chung, K. Cho, Z. Kan, H. Liu, X. Lu, Y. Lang, H. Lai, F. He, P.W.K. Fong, S. Lu, Y. Yang, Z. Xiao, G. Li, Nat. Commun. 15 (2024) 1830.
[7] J. Xie, J. Zhao, Z. Zhou, K. Zhang, J. Yu, C. Zhu, F. Huang, Energy Environ. Sci. 17 (2024) 7681–7690.
[8] Y. Yang, C. Liu, J. Xu, C. Huang, C.D. Malliakas, H. Wan, A.S.R. Bati, Z. Wang, R.P. Reynolds, I.W. Gilley, S. Kitade, T. Wiggins, S. Zeiske, S. Suragtkhuu, M. Batmunkh, L.X. Chen, B. Chen, M.G. Kanatzidis, E.H. Sargent, Science 386 (2024) 898–902.
[9] S. Rahmany, L. Etgar, ACS Energy Lett. 5 (2020) 1519–1531.
[10] B. Shi, L. Duan, Y. Zhao, J. Luo, X. Zhang, Adv. Mater. 32 (2020) 1806474.
[11] H. Wu, Y. Cheng, J. Ma, J. Zhang, Y. Zhang, Y. Song, S. Peng, Adv. Mater. 35 (2023) 2206574.
[12] Y. Cui, C. Yang, H. Yao, J. Zhu, Y. Wang, G. Jia, F. Gao, J. Hou, Adv. Mater. 29 (2017) 1703080.
[13] F. Liu, Z. Zhou, C. Zhang, J. Zhang, Q. Hu, T. Vergote, F. Liu, T.P. Russell, X. Zhu, Adv. Mater. 29 (2017) 1606574.
[14] F.C. Krebs, N. Espinosa, M. Hosel, R.R. Sondergaard, M. Jorgensen, Adv. Mater. 26 (2014) 29–38.
[15] H. Shi, R. Xia, G. Zhang, H.L. Yip, Y. Cao, Adv. Energy Mater. 9 (2019) 1803438.
[16] C. Sun, R. Xia, H. Shi, H. Yao, X. Liu, J. Hou, F. Huang, H.-L. Yip, Y. Cao, Joule 2 (2018) 1816–1826.
[17] D. Wang, H. Liu, Y. Li, G. Zhou, L. Zhan, H. Zhu, X. Lu, H. Chen, C.-Z. Li, Joule 5 (2021) 945–957.
[18] D. Wang, Y. Li, G. Zhou, E. Gu, R. Xia, B. Yan, J. Yao, H. Zhu, X. Lu, H.-L. Yip, H. Chen, C.-Z. Li, Energy Environ. Sci. 15 (2022) 2629–2637.
[19] Z. Hu, J. Wang, X. Ma, J. Gao, C. Xu, K. Yang, Z. Wang, J. Zhang, F. Zhang, Nano Energy 78 (2020) 105376.
[20] G.P. Kini, S.J. Jeon, D.K. Moon, Adv. Funct. Mater. 31 (2021) 2007931.
[21] X. Huang, X. Ren, Y. Cheng, Y. Zhang, Z. Sun, S. Yang, S. Kim, C. Yang, F. Wu, L. Chen, Energy Environ. Sci. 17 (2024) 2825–2836.
[22] Y.X. Huang, Y. Cheng, Y. Fang, L. Zhang, X. Hu, S.Y. Jeong, H. Zhang, H.Y. Woo, F. Wu, L. Chen, Energy Environ. Sci. 15 (2022) 4776–4788.
[23] J. Ding, H. Mou, H. Chen, J. Xu, W. Sun, J. Zhu, Y. Wang, Y. Huang, Y. Li, Y. Li, Adv. Mater. 37 (2025) 2420436.
[24] J. Zhang, G. Xu, F. Tao, G. Zeng, M. Zhang, Y.M. Yang, Y. Li, Y. Li, Adv. Mater. 31 (2019) 1807159.
[25] G. Xu, L. Shen, C. Cui, S. Wen, R. Xue, W. Chen, H. Chen, J. Zhang, H. Li, Y. Li, Y. Li, Adv. Funct. Mater. 27 (2017) 1605908.
[26] R. Xia, C.J. Brabec, H.-L. Yip, Y. Cao, Joule 3 (2019) 2241–2254.
[27] Y. Zhang, J. Zheng, Z. Jiang, X. He, J. Kim, L. Xu, M. Qin, X. Lu, A.K.K. Kyaw, W.C. H. Choy, Adv. Energy Mater. 13 (2023) 2203266.
[28] Y. Li, C. Ji, Y. Qu, X. Huang, S. Hou, C.Z. Li, L.S. Liao, L.J. Guo, S.R. Forrest, Adv. Mater. 31 (2019) 1903173.
[29] B. Deng, K. Zheng, Z. Wang, L. Yin, H. Dong, C. Zhang, M. Treguer-Delapierre, K. N'konou, B. Grandidier, S. Wang, J. Zhang, T. Xu, ACS Energy Lett. 9 (2024) 976–984.
[30] F. Xue, Y. Xie, Y. Cui, D. Yu Paraschuk, W. Ma, H. Yan, Adv. Funct. Mater. 35 (2025) 2415617.

[31] T. Xu, Y. Luo, S. Wu, B. Deng, S. Chen, Y. Zhong, S. Wang, G. Leveque, R. Bachelot, F. Zhu, Adv. Sci. 9 (2022) 2202150.
[32] Y. Xie, Y. Cai, L. Zhu, R. Xia, L. Ye, X. Feng, H.L. Yip, F. Liu, G. Lu, S. Tan, Y. Sun, Adv. Funct. Mater. 30 (2020) 2002181.
[33] P.O. Amin, F.F. Muhammadsharif, S.R. Saeed, K.A. Ketuly, Sustainability 15 (2023) 12442.
[34] Y. Zhang, D. Luo, C. Shan, Q. Liu, X. Gu, W. Li, W.C.H. Choy, A.K.K. Kyaw, Sol. RRL 6 (2021) 2100785.
[35] X. Wang, X. Zhai, X. Kang, X. Ding, C. Gao, X. Jing, L. Yu, M. Sun, Sol. RRL 6 (2022) 2200070.
[36] Z. Wu, B. Shi, J. Yu, M. Sha, J. Sun, D. Jiang, X. Liu, W. Wu, Y. Tan, H. Li, S. Huang, J. Wang, J. Liu, C. Zhang, X. Ma, L. Cui, L. Ye, F. Zhang, B. Cao, Y. Chen, Z. Ji, F. Chen, X. Hao, G. Li, H. Yin, Energy Environ. Sci. 17 (2024) 6013–6023.
[37] J. Xie, W. Lin, K. Zheng, Z. Liang, Adv. Sci. 11 (2024) 2404135.
[38] M. Kaltenbrunner, M.S. White, E.D. Glowacki, T. Sekitani, T. Someya, N.S. Sariciftci, S. Bauer, Nat. Commun. 3 (2012) 770.
[39] A. Sharma, N. Gasparini, A. Markina, S. Karuthedath, J. Gorenflot, H. Xu, J. Han, A. Balawi, W. Liu, D. Bryant, J. Bertrandie, J. Troughton, S.H.K. Paleti, H. Bristow, F. Laquai, D. Andrienko, D. Baran, Adv. Mater. 36 (2024) 2305367.
[40] Y. Tamai, Y. Fan, V.O. Kim, K. Ziabrev, A. Rao, S. Barlow, S.R. Marder, R.H. Friend, S.M. Menke, ACS Nano 11 (2017) 12473–12481.
[41] M.C. Scharber, D. Mühlbacher, M. Koppe, P. Denk, C. Waldauf, A.J. Heeger, C.J. Brabec, Adv. Mater. 18 (2006) 789–794.
[42] G. Han, Y. Yi, Adv. Theory Simul. 2 (2019) 1900067.
[43] G.D. Scholes, G. Rumbles, Nat. Mater. 5 (2006) 683–696.
[44] S. Brazovskii, N. Kirova, Chem. Soc. Rev. 39 (2010) 2453–2465.
[45] L. Zhu, Z. Wei, Y. Yi, J. Phys. Chem. C 126 (2021) 14–21.
[46] Y. Lin, Y. Firdaus, F.H. Isikgor, M.I. Nugraha, E. Yengel, G.T. Harrison, R. Hallani, A. El-Labban, H. Faber, C. Ma, X. Zheng, A. Subbiah, C.T. Howells, O.M. Bakr, I. McCulloch, S.D. Wolf, L. Tsetseris, T.D. Anthopoulos, ACS Energy Lett. 5 (2020) 2935–2944.
[47] S. Guan, Y. Li, K. Yan, W. Fu, L. Zuo, H. Chen, Adv. Mater. 34 (2022) 2302927.
[48] C.M. Proctor, M. Kuik, T.-Q. Nguyen, Prog. Polym. Sci. 38 (2013) 1941–1960.
[49] V. May, J. Chem. Phys. 140 (2014) 054103.
[50] K. Kanemoto, S. Domoto, H. Hashimoto, J. Phys. Chem. C 118 (2014) 17260–17265.
[51] T.A. Dela Peña, J.I. Khan, N. Chaturvedi, R. Ma, Z. Xing, J. Gorenflot, A. Sharma, F. L. Ng, D. Baran, H. Yan, F. Laquai, K.S. Wong, ACS Energy Lett. 6 (2021) 3408–3416.
[52] X.-K. Chen, D. Qian, Y. Wang, T. Kirchartz, W. Tress, H. Yao, J. Yuan, M. Hülsbeck, M. Zhang, Y. Zou, Y. Sun, Y. Li, J. Hou, O. Inganäs, V. Coropceanu, J.-L. Bredas, F. Gao, Nat. Energy 6 (2021) 799–806.